



HAL
open science

Shadowgraphy investigation of the combustion of raw and pre-treated single biomass particles: Influence of particle size and volatile content

Hassan Mohanna, Jean-Michel Commandre, Bruno Piriou, Gilles Vaitilingom, Benoît Taupin, David Honoré

► **To cite this version:**

Hassan Mohanna, Jean-Michel Commandre, Bruno Piriou, Gilles Vaitilingom, Benoît Taupin, et al.. Shadowgraphy investigation of the combustion of raw and pre-treated single biomass particles: Influence of particle size and volatile content. *Fuel*, 2019, 258, pp.116113. 10.1016/j.fuel.2019.116113 . hal-02311538

HAL Id: hal-02311538

<https://hal.science/hal-02311538>

Submitted on 23 Dec 2020

HAL is a multi-disciplinary open access archive for the deposit and dissemination of scientific research documents, whether they are published or not. The documents may come from teaching and research institutions in France or abroad, or from public or private research centers.

L'archive ouverte pluridisciplinaire **HAL**, est destinée au dépôt et à la diffusion de documents scientifiques de niveau recherche, publiés ou non, émanant des établissements d'enseignement et de recherche français ou étrangers, des laboratoires publics ou privés.

Shadowgraphy Investigation of the Combustion of Raw and Pre-treated Single Biomass Particles: Influence of Particle Size and Volatile Content

Hassan MOHANNA¹⁻³, Jean-Michel COMMANDRE¹,
Bruno PIRIOU¹, Gilles VAITILINGOM¹, Benoit TAUPIN², David HONORE³
¹ CIRAD UPR BioWooEB, 34398 Montpellier, France
² Veolia Recherche et Innovation (VeRI), 78520 Limay, France
³ Normandie Univ, INSA Rouen, UNIROUEN, CNRS, CORIA, 76000 Rouen, France

Abstract

An experimental study of single particle combustion is performed in a high temperature particle reactor. The particle degradation is simultaneously monitored by high magnification direct imaging and by shadowgraph imaging techniques giving access to the full behaviour of the particle even when enveloped by a flame. This allows tracing the time-resolved evolution of the particle shadow during its degradation as a function of its burnout. The method provides access to the whole process timeline, especially the onset of the heterogeneous oxidation even during the flame phase. It is observed to occur earlier for larger particles containing lower volatile matter. The latter occupies around 40% of the initial particle shadow, which decreases with devolatilisation progress following a power trend. The char burns at the surface until the reaction front penetrates the particle leaving an ash matrix behind. Effects of particle size and volatile matter on the different steps of particle combustion are discussed. Moreover, biomass behaviour is compared to that of coal. The whole results give new insights in the combustion of single biomass particle and are available for the development and validation of dedicated solid fuel combustion models.

Introduction

In the view of the polluting role of coal, incorporating a fraction of biomass into coal in pulverized burners can be an effective environmental strategy. However, this significantly modifies the functionality of the installations considering the different combustion behaviour of biomass at flame and particle level [1]. However, unlike coal which has been extensively studied by the scientific community given its influential role in the industrial revolution, the integration of biomass in industry is more recent, and more research is required to improve the available technology.

Single particle reactors are successfully employed for coal in literature using heated grid reactor, batch type reactors, free fall and entrained flow reactors, etc. [1]–[4]. In general, the experimental rigs consist basically of a heated chamber in which a particle is introduced at high temperature to record its degradation. The particle can be suspended on a fixed support or in a free stream according to the size.

This kind of experiments is necessary to validate the theoretical concepts describing the phenomena and to examine the related parameters of the process conditions. However, fewer studies adapted these reactor to biomass [5]–[9]. Lu et al. [8] demonstrated in such experiment on biomass that shape and aspect ratio differences show measurable differences in pyrolysis rates. Schiemann et al. [5], [10] also concluded to the same result using a new stereoscopic pyrometer to measure the particle temperature and shape at the same time in a laminar flow reactor. Momeni et al. [6] reported that the ignition delay of a stationary particle

39 is clearly influenced by the oxygen concentration in the surrounding atmosphere. Similar aspects were
 40 assessed by Houshfar et al. [9] using gas emissions of single particles. These results serve to translate the
 41 combustion stage into empirical expressions that can be integrated in physical models [8], [11], [12]. Beside
 42 the combustion behaviour, some studies examined the impact of fuel pre-treatment. Lu et al. [7] pointed
 43 out that torrefaction shortens the devolatilization time while increasing the char yield and density. Riaza et
 44 al. [3] also reported that increasing oxygen mole fraction in ambient atmosphere reduces the surrounding
 45 flame luminosity.

46 The objective of this study is to provide additional insight to the combustion timeline of a single particle
 47 of biomass using imaging techniques. Direct visible imaging is performed to visualize particle combustion.
 48 Moreover, shadowgraphy is employed to trace simultaneously the particle projection area and shape
 49 evolution. Incorporating both techniques with the temperature measurement provides fundamental data on
 50 the events corresponding to each involved phenomenon. The investigation examines the impact of
 51 torrefaction and particle size on the combustion behaviour.

52 1. Fuel composition and properties

53 The fuels are selected in the purpose of investigating the volatile matter (VM) content influence on the
 54 combustion process. Pine is chosen as a reference biomass and is torrefied at 280 °C for 25 min to produce
 55 pint and also partially pyrolyzed at 450 °C for 15 min to produce pinp. A longer residence time of 20 min
 56 at 450 °C released more volatiles and produced carbonized pine (denoted pinc). The thermal preparation of
 57 the received wood chips was done in a heated screw reactor under nitrogen inert atmosphere. Demolition
 58 wood (DW) is also used as representative of waste fuels.

	<i>pine</i>	<i>pint</i>	<i>pinp</i>	<i>pinc</i>	<i>DW</i>	<i>Coal</i>
<i>Ash</i>	0.87	1.33	2.54	3.24	2.13	2.03
<i>VM</i>	81.22	73.62	44.83	19.59	78.29	37.08
<i>FC</i>	18.58	25.05	52.62	77.17	19.57	60.89
<i>C</i>	51.68	55.10	67.77	79.87	48.51	82.14
<i>H</i>	5.93	5.68	4.50	3.44	5.63	5.57
<i>N</i>	0.22	0.29	0.32	0.39	4.39	1.54
<i>O</i>	41.27	37.52	25.15	16.28	40.58	8.71
<i>LHV</i> (MJ/kg)	18.45	19.744	25.30	28.33	17.70	32.34

59 **Table 1:** Fuel composition analysis (%db)

	<i>pine</i>	<i>pint</i>	<i>pinp</i>	<i>pinc</i>	<i>DW</i>	<i>Coal</i>
Particle shape	<i>Needle-like</i>	<i>cylindrical</i>	<i>cylindrical</i>	<i>Near-spherical</i>	<i>Flake-like</i>	<i>Near-spherical</i>
Aspect ratio	2.50±0.70	1.67±0.40	1.65±0.41	1.41±0.29	2.08±0.48	1.28±0.26
Particle size (mm) (min-max)	0.68-1.57	0.42-1.15	0.49-1.25	0.49-1.02	0.50-1.74	0.48-0.93
Mass (mg) (min-max)	0.1-1.8	0.1-1.3	0.1-1.1	0.1-1.1	0.5-2.1	0.6-1.6
Number of tested particles	32	29	30	16	31	25

60 **Table 2:** Physical appearance of the tested particles

61 In addition, Venezuelan coal was tested aiming to show the different behaviour of combustion of biomass
 62 and a coal even when containing a high volatile content. The proximate and ultimate analyses of the fuel
 63 are listed in **Table 1** obtained following the ASTM norms. **Table 2** shows the physical properties (shape
 64 and size) of the tested particles of each tested fuel. Fuels are grounded thanks to a knives mill with a 1.5
 65 mm sieve. The size of the particles obtained after grinding is in the range 0.4 and 2 mm possessing different
 66 aspect ratios and their mass is up to maximum 2 mg. Pine particles are mostly needle-like while torrefied
 67 pine and coal are between cylindrical and spherical particles. Demolition wood particles are mostly thick
 68 flakes made of small compressed fragments of wood.

69 2. Experimental methods

70 2.1. Single particle combustion apparatus

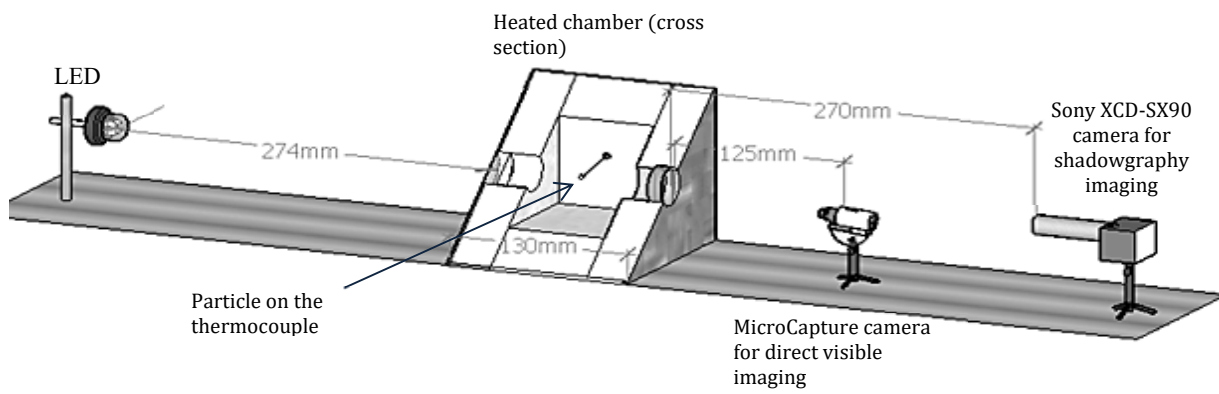


Figure 1: Particle combustion shadowgraphy experimental apparatus

71
 72 An experimental apparatus is designed to monitor the shadow of a solid particle during its thermal
 73 conversion [13]. The setup in **Figure 1** consists of a 12 x 13 x 14 cm heated combustion chamber fixed on
 74 a horizontal bench alongside with two cameras and a LED lamp. The chamber is electrically heated to a set
 75 point of 800 °C maximum and maintained at the set temperature with the help of an isolation layer. Two
 76 optical windows are situated on opposite sides of the chamber. These 3cm-dia. windows beside the small
 77 sizes of the cameras were sufficient to place both of them on the same side at long distance from the chamber
 78 to limit non-paraxial effect. The monochrome camera (Sony XCD-SX90) for shadowgraphy imaging is
 79 equipped with Navitar precise eye lens, 0.25x lens attachment to increase the working distance, and 2.0x
 80 adapter producing suitable magnification (0.4 $\mu\text{m}/\text{pixel}$). The camera is adjusted to capture images
 81 (850x850 pixel²) at 37 fps with 0.2 ms exposure time. Another camera (MicroCapture) records at 30 fps
 82 visible color images (352x288 pixel²) with an optical zoom giving a magnification ratio of 4.16 $\mu\text{m}/\text{pixel}$.
 83 Both cameras are held at a fixed distance from the particle position to achieve a consistent optical
 84 magnification and similar line-of-sight. The background is lighted with a collimated illumination generated
 85 by a LED lamp on the same axis of the particle for shadowgraphy measurements. The advantage of this
 86 technique is that it can surpass the flame barrier during the combustion of volatiles and access the full

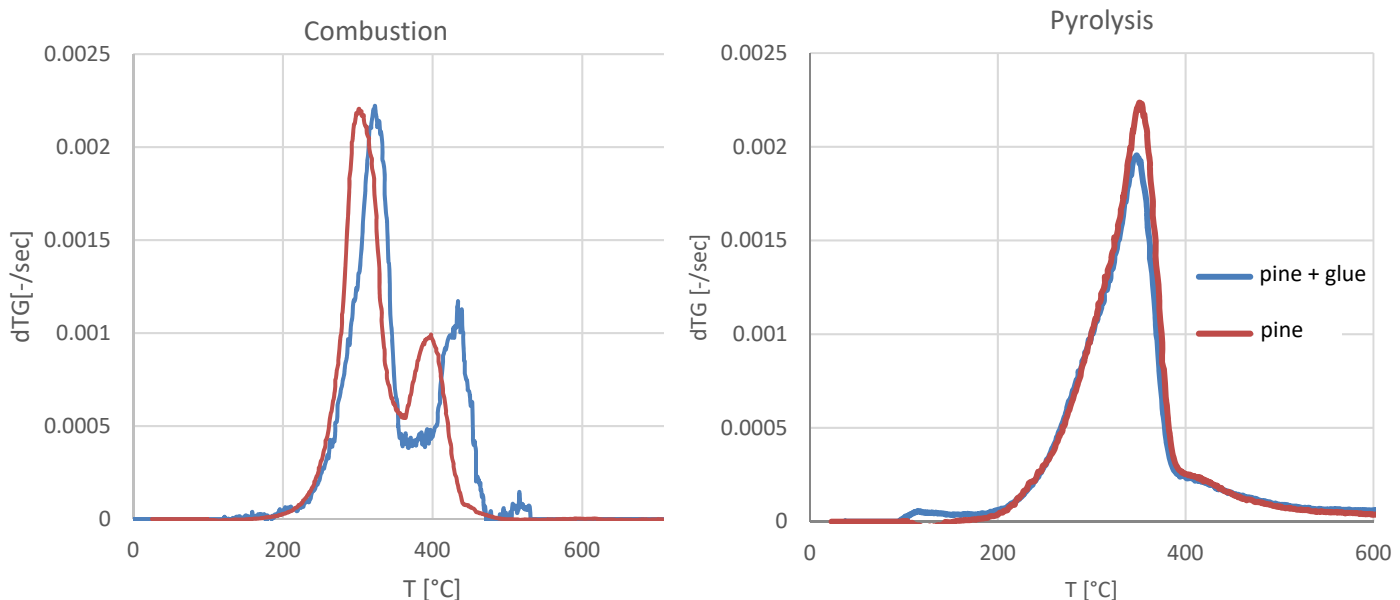
87 particle shape and volume evolution with time that is not available with usual direct visible imaging
88 techniques.

89 2.2. Methodology

90 The samples are dried for 24 hours before every experiment considering the high variation in moisture
91 content Moisture: 13% pinp, 1.9% pint, which can hugely influence the particles behaviour and ignition
92 delay. A significant number of particles are tested for each fuel to reduce the deviations and better determine
93 the trends and average values (table 2).

94 Prior to an experiment, a particle is glued to the tip of a 250 μm thermocouple measuring the surface
95 temperature at a temporal frequency of 12 Hz. The glue is a high-temperature nonorganic paste used in a
96 very small quantity at the position of the particle and left to dry to ensure little interference with the
97 occurring thermochemical phenomena. As the biomass is tested with glue, dedicated experiments have been
98 performed to determine if an influence of glue can be noticed on reaction kinetics. This potential influence
99 is evaluated by comparing the thermogravimetric analysis of a sample of particles covered from one side
100 with the glue and held in a wide crucible, and a reference sample of pine without glue in **Figure 2**. Under
101 inert atmosphere, it seems to have little effect on the pyrolysis behaviour. However, the combustion tests
102 revealed that the glue shifts slightly the degradation peaks to a higher temperature and separate the char
103 and volatile oxidation process. Little to negligible difference on the conversion peaks values, processes
104 durations, and ignition temperature is observed in comparing both curves. So, the effect of the glue is
105 limited and it allows the comparison of results obtained with different fuels using same methodology.

106 **Figure 2:** TGA profiles showing the influence of glue on the combustion of pine



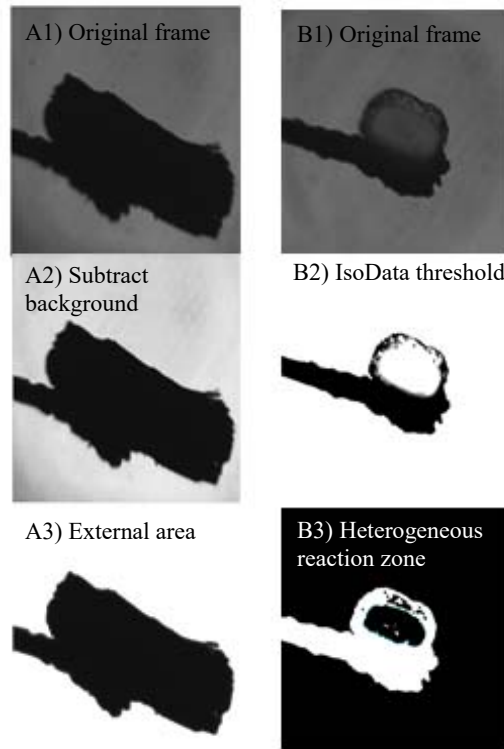
107 Once the chamber attains and stabilizes at the experiment temperature, the particle is inserted quickly to
108 the hot medium by the help of a guiding rod fixed to the external wall of the chamber. The particle position
109 is adjusted to be always in the field of view of both cameras during the whole process.

110 2.3. Processing of simultaneous time-series of images

111 Shadowgraph monochrome images are binarised in order to facilitate the detection of the particle
112 contours (**Figure 3** - A1 and B1). The background is subtracted using the rolling ball algorithm creating
113 black objects on a smooth continuous background in **Figure 3** -A2 [14]. In the progress of its combustion,
114 the particle luminosity changes after the flame extinguishes due to char radiation. Therefore, it is necessary
115 to apply a threshold method for the flame stage followed by another for the char combustion part. During
116 the flame stage we used an iterative procedure based on the IsoData algorithm (**Figure 3** -A3) [16]. For the
117 char combustion part, the external contour was more difficult to detect as the threshold depends strongly
118 on the particle luminosity, which varies with time and particle nature. The particle luminosity was similar
119 to that of the background, so the algorithm was highlighting it in white surrounded by the particle edges as
120 shown in **Figure 3** (B2). Indeed, the white inner zone here is the bright region of the particle where the
121 heterogeneous reaction takes place, while the surrounding black region is the burnt part (ash). It is
122 noticeable how the reaction zone during the char combustion separates from the external area of the particle
123 and undergoes internal combustion. Hence, the IsoData method was repeated in this stage with additional
124 treatment and the purpose this time was to follow the evolution of the reaction bright zone, which is directly
125 related to the progress of the heterogeneous combustion. Colors were inverted to keep the detection zone
126 in black for the contour detection later. Further treatment including automatic dilating and filling holes was
127 performed to distinguish as much as possible the zone of interest (B3).

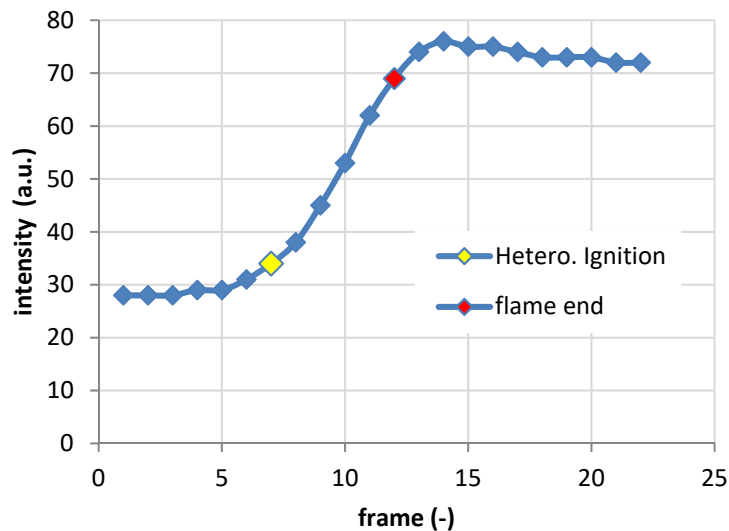
128 Moreover, the external area at this stage are extracted using the Mean method that fits best the data among
129 seventeen tested methods [15]. The images are then processed by a contour detection program capable of
130 generating the evolution curve of the projection area of the particle as a function of time [16]. The code can
131 detect the thermocouple and subtract it from the calculation. In order to subtract the glue area and eliminate
132 the sensitivity of the thresholding process, the curves were then rectified by manually integrating several
133 points on each curve and account for the error.

134 The two image series and the thermocouple data are zeroed at the insertion moment in order to have a
135 synchronicity between the temporal data. Superposition of the data helps to identify the events associated
136 to each phenomenon. Moreover, superposing both imaging techniques provides the moment of the onset of
137 heterogeneous combustion even during the flame phase. In fact, the combustion sub-processes occur
138 simultaneously at high heating rates, but the overlap of homogenous and heterogeneous combustion is
139 difficult to evaluate experimentally. However, using shadowgraphy, the particle can be monitored
140 throughout the whole combustion experiment. The moment oxygen attacks the char surface is associated
141 with a slight brightness at that position. The luminosity is really clear after the flame is completely
142 extinguished but it can be also traced back on shadow images to its onset during the flame period, while
143 the flame still appears to radiate on the direct visible images at the same time.



144
145
146

Figure 3: Image treatment for the contour detection of the external area of a particle during devolatilisation (left) and the heterogeneous reaction zone (right)



147
148

Figure 4: Brightness increase on shadow images at the heterogeneous ignition position

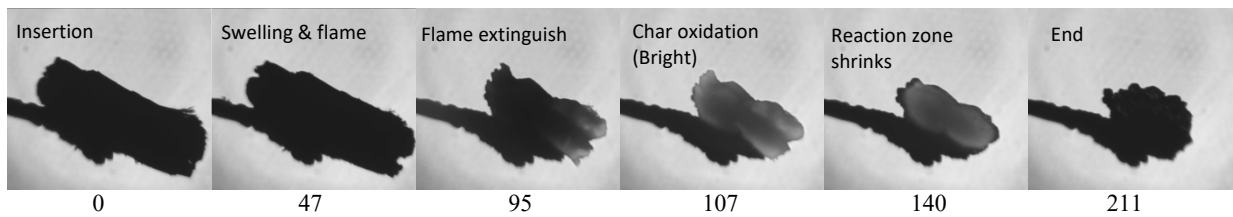
149 The curve in **Figure 4** follows the intensity at the surface of a pine particle. The particle brightness is quite
150 constant before frame 6 (yellow marker) where the intensity commences to increase afterwards till it
151 becomes very bright after the flame extinguishes in frame 11. This increase in intensity at the char surface
152 is then considered as the heterogeneous ignition moment. Once identified, the time difference until the
153 flame extinguishes is defined as the homo-hetero overlap.

154 **2.4. Visual observation of the combustion**

155 A general trend of particle behaviour is observed for biomass. A typical size evolution of a biomass particle
156 with time is presented as a series of images in **Figure 5** and the corresponding time evolution of particle
157 area in **Figure 6**. After its insertion to the hot zone, a series of events is triggered. The particle swells for a
158 certain moment due to the increasing pressure of volatiles inside it. The swelling coefficient depends on the
159 biomass type: it is longer for pine than for pint whereas it is negligible for pinp.

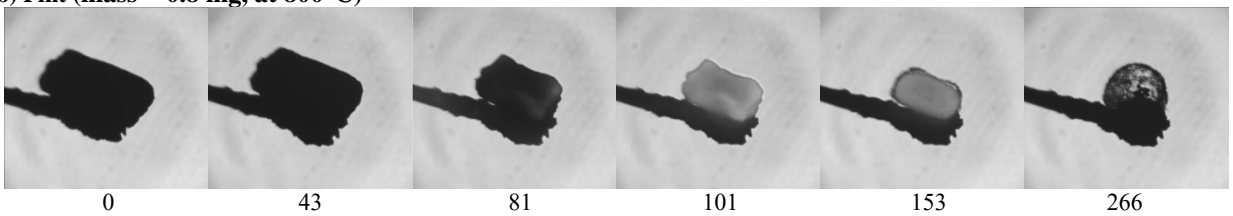
160

161 **a) Pine (mass = 1.3 mg, at 800°C)**

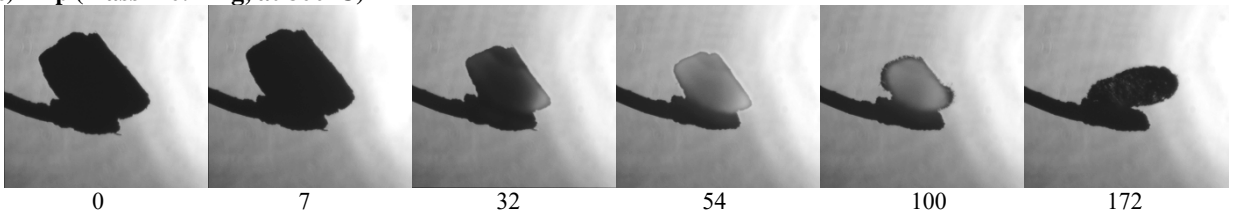


166
167
168
169

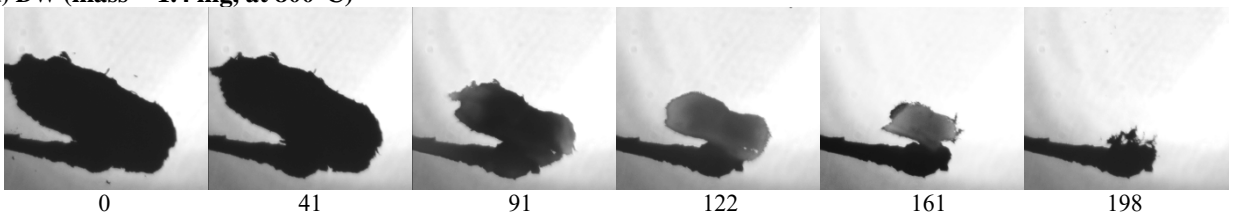
b) Pint (mass = 0.8 mg, at 800°C)



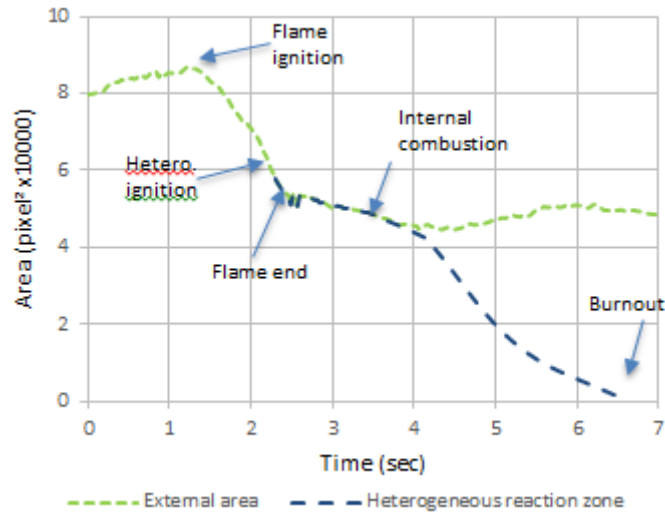
c) Pinp (mass = 0.4 mg, at 800°C)



d) DW (mass = 1.4 mg, at 800°C)



178 **Figure 5:** High magnification shadow images of the combustion of single particles of raw pine, torrefied
179 pine, pyrolyzed pine and demolition wood. The displayed number for each image is the frame number
recorded at 37 fps from the insertion moment



180
181

Figure 6: Typical size evolution of biomass with time

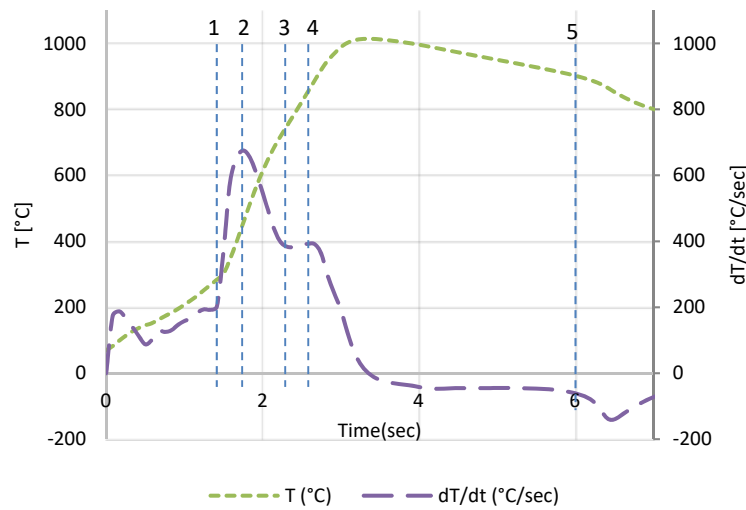
182 The swelling is followed by a flame accompanied by rapid decrease in particle size due to the liberation of
 183 volatiles that rapidly react to produce the surrounding flame with characteristics dependent on the VM
 184 content within the particle. The flame intensity and size increase with time and then shrinks back until its
 185 extinction. Around 40% of the initial projection area is lost during this step, which corresponds to the
 186 volume loss due to the volatile content release. Particle consumption then slows down after the flame
 187 extinguishes. The char becomes bright glowing red by the effect of carbon oxidation. At first, the particle
 188 shrinks with the luminous region signifying the oxidation at the surface of the particle. A point of separation
 189 between the reaction zone (bright zone) and the external area is detected (denoted as reaction zone shrinks
 190 in **Figure 5**). The reaction front continues to travel inside the particle (internal combustion) leaving a dark
 191 zone behind until the complete burnout. The heterogeneous reaction zone curve in **Figure 6** follows the
 192 bright zone that separates at a certain moment from the external area curve. The result is a hollow particle
 193 of ash that swells sometimes at the end. Fragmentation of the particle is also sometimes observed especially
 194 for DW.

195 2.5. Temperature-time history of biomass particles

196 Similar to area evolution, a trend of temperature profile is observed for biomass during their burnout history.
 197 **Figure 7** presents the temperature and its derivative (dT/dt) with time which is the result of the energy
 198 balance of the particle. The insertion is at $t = 0$ sec in synchronicity with images recordings. We assume
 199 that the limitation of heat transfer through the glue is negligible, as well as the influence of radiation on the
 200 thermocouple, so the measured temperature of the thermocouple is representative of that of the particle.

201 The temperature derivative peaks at three events: upon insertion and rapid heating, maximum flame size,
 202 and when the flame is blown out. The flame was detected visually in the two image series, when the volatile
 203 cloud around the particle is lit, and by the sudden increase in the surface temperature profile giving the
 204 ignition temperature shown as event #1 on **Figure 7**. The second peak – event #2 - corresponds to the

205 devolatilization peak where dT/dt decreases afterwards due to lower volatile emission rate. This is also
206 obtained in TGA experiments by the DTG peak and oxygen consumption peak [17].



207
208 **Figure 7:** Temperature variation of biomass particle during combustion. The corresponding events (1-5)
209 are detailed in the text.

210 The peak value declines with increasing particle mass, which suggests that lighter particles undergo intense
211 pyrolysis. dT/dt reduction arrives to a local minimum (event #3), which coincides with the heterogeneous
212 ignition detected by the previously mentioned technique. The char combustion heats the particle without
213 losing significant heat to the high temperature surrounding flame. Once the volatile flame quenches, the
214 particle starts losing heat, whence the second chute. The peak of event #4 is then attributed to the flame
215 extinguishment. Sometimes a shorter overlap between the volatile and char combustion makes this peak
216 less pronounced. A significant difference between the wall (800°C) and particle temperatures reverses the
217 heat flow direction after the particle reaches its maximum temperature. Subsequently, a balance is
218 established between the energy production and loss until the complete burnout, which is characterized by
219 a third decrease – event #5 - with no more energy production. The temperature then stabilizes at the chamber
220 temperature (800°C).

221 3. Combustion durations

222 3.1. Ignition delay

223 The ignition of biomass particles is in general initiated in the gas phase. The combustion reaction is
224 activated when the volatile cloud around the particle acquires sufficient energy and flammable
225 concentration. The two entities are properties of the volatile gas composition and the heat capacity of the
226 surrounding gas [3]. The TGA curves showed that the devolatilisation commences early (at 221 °C for pine)
227 and it can be detected in the shadowgraph image time-series by the sudden decrease in the particle volume
228 after building internal pressure. The delay between the release of volatiles and their ignition is so short that
229 they appear simultaneously at 37 frame/sec recording. The ignition delay is defined by the time needed to

230 have a rapid temperature rise after the insertion of the particle. TGA curves are usually used to identify the
 231 ignition temperature of biomass. Previous investigations pointed out that the ignition delay times increased
 232 with the increase of the initial particle density and diameter. Nevertheless, TGA conclusions cannot be
 233 extrapolated for high heating rates conditions. Li et al. [18] found that torrefied softwood was faster to
 234 ignite than raw softwood at high heating rates. The authors addressed that by the change in ignition
 235 mechanism from homogenous to heterogeneous ignition promoted by higher char reactivity of torrefied
 236 biomass. Moreover, at high heating rates, the volatiles are easily driven out of high porous particles with
 237 barely any swelling detected as in the case for pinp, while the swelling of raw particles implies that the
 238 volatile release is delayed until acquiring sufficient pressure to break the particle wall structure.

Fuel	Pine	Pint	Pinp	Pinc	DW
Ignition temperature (°C)	240 ± 11	290 ± 22	220 ± 26	346 ± 14	258 ± 41

239 **Table 3:** Ignition temperature of the tested fuels

240 The ignition temperatures measured in the present experiments are shown in **Table 3**. Raw pine ignites at
 241 240 °C, which is close to the temperature reported in [19] for beech wood (235°C). Demolition wood ignites
 242 at around 258 °C with high variations ($\pm 41^\circ\text{C}$) due to the presence of impurities and high particle-to-
 243 particle variations. The improved hydrophobicity of torrefied fuel generally reduces its ignition delay
 244 compared to high moisture raw counterpart [11], [20]. In this study, the fuels were dried before the
 245 experiments, so the influence of moisture is eliminated and the conclusions are purely based on the particle
 246 properties. Pint flame appeared at 290 °C due to lower volatile concentration. Despite its poor VM content,
 247 pinp ignites even before raw pine at 220 °C where the ignition is dominated by the higher porosity and
 248 improved reactivity of pinp. The release of pyrolytic water during torrefaction and the significantly lower
 249 density may also have a role in improving the ignitability of the pinp volatiles. In all cases, the presence of
 250 volatiles facilitates the ignition at relatively low temperatures while for no flame is visible for the low VM
 251 carbonized pine and the heterogeneous ignition is delayed until the particle reaches 346 °C.

252 3.2. Volatile flame duration

253 **Figure 8**,a plots the flame duration as a function of the particle mass. The quasi linear increase is logical
 254 since more volatiles require more time to burn [21]. Besides, bigger particle's temperature rises slower than
 255 finer particle one at the same heating conditions. This slows down the devolatilisation rate. However, little
 256 to no difference is detected between the flame durations of different fuel types. Only, pinp flame duration
 257 appears shorter than the other flames due to relatively low volatile content. Akinrinola et al. [20] reported
 258 a similar result of close flame duration for raw and torrefied Nigerian biomass. It was however reported
 259 longer by 10-15% in the torrefied state for Miscanthus and Beech wood in [22]. The authors attributed this
 260 effect to the increasing influence of the catalytic metals in the fuels. It is also possible that the new pores
 261 created during torrefaction facilitate the emission of volatiles. In this case, the flux of volatile emission is

262 lower for the treated biomass, which elongates their emission time in comparison to time needed for same
263 amount of volatiles in their raw counterparts.

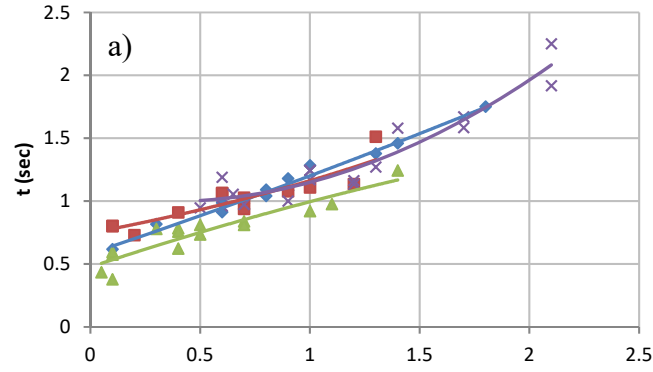
264 **3.3. Homo-hetero combustion overlap**

265 The overlap of flame combustion and char combustion is introduced in **Figure 8,b**. Note that the points
266 only represent the particles that their heterogeneous ignition observed on shadow images coincides with
267 the local minimum in the temperature derivative curve. In the other case, the difference between the
268 luminosity detection and the (dT/dt) local minimum for some particles may be addressed by the fact that
269 the ignition may be triggered from the backward side of the particle so that the temperature derivative
270 minimum appears earlier than predicted by the rear view.

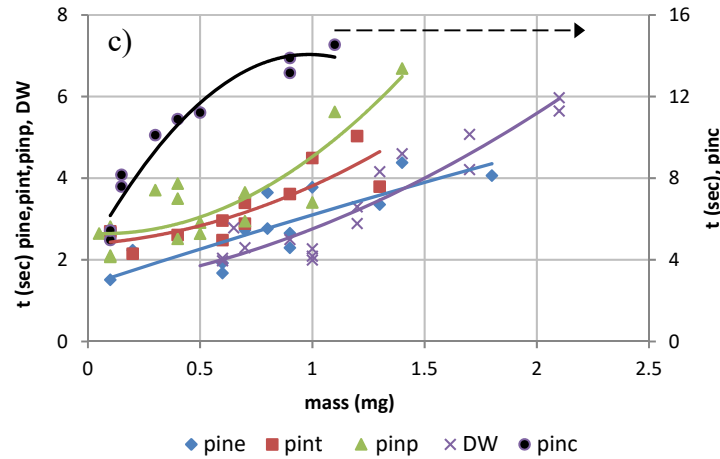
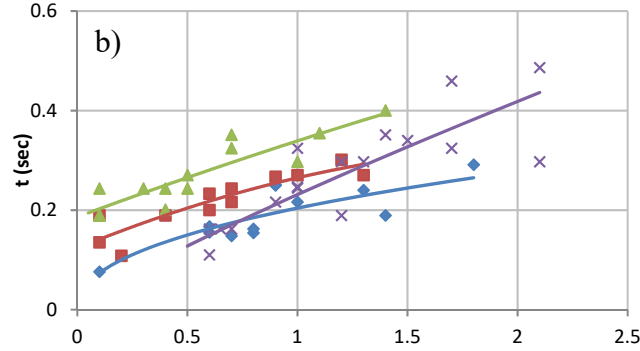
271 The heterogeneous ignition occurs earlier for larger particles containing lower volatile content, and thus
272 increases the overlap duration. Torrefaction of pine induces an increase of overlap duration. The maximum
273 overlap among the pine-derived fuels was obtained for pinp with 0.4 sec for a 1.4 mg particle. On the other
274 hand, a 0.1 mg pine particle had the minimum overlap of 0.076 sec. When the particle is surrounded by
275 flame, the temperature is high enough for the heterogeneous ignition to happen. The heterogeneous ignition
276 of carbonized pine starts at significantly lower temperatures. Nonetheless, the lack of oxygen at the surface
277 induces a delay in the ignition. This may occur early for a particle in a free stream where the motion of the
278 irregularly shaped particle exposes an edge to the hot stream out of the spherical flame envelope. Mock et
279 al. [23] in these conditions observed overlap taking place in the last 40% of the flame duration for coffee
280 waste and sewage sludge particles (150-215 μm). On the other hand, the more spherical treated wood
281 experienced a relatively short overlap (9% of flame duration). However, for a stationary particle in the
282 current study, the char undergoes ignition while enveloped by a flame. Therefore, the ignition here is
283 controlled by the diffusion of oxygen to the surface through the volatile cloud without being consumed or
284 diverted away. Larger particles have larger surface area and therefore it is more probable for them to receive
285 locally more oxygen than smaller ones. This explains why larger particles of the same fuel present char
286 ignition earlier. The same analysis may apply in explaining why the overlap increases with the torrefaction
287 degree. Torrefaction reduces the particle density so that a raw particle of the same mass as a torrefied one
288 has larger size, and thus higher overlap. Moreover, the outward flow of volatile matter seems to obstruct
289 the molecular diffusion of oxygen towards the particle surface. Results show that the volatile flow tends to
290 be more intense with smaller particles and with more VM. Therefore, the probability of oxygen passing the
291 volatile cloud to react with the char is lower for smaller particles and for higher VM content so that the
292 probability of ignition is lower.

293

294



295



296
297

Figure 8: Combustion durations: a) flame; b) overlap; c) burnout

298 3.4. Burnout time

299 The higher overlap between the flame phase and char combustion phase shortens the total burnout duration.
 300 **Figure 8,c** shows the total burnout duration of each biomass from the moment of ignition to the total
 301 consumption of the particle. An increasing tendency of combustion duration versus mass is measured for
 302 all fuels. Lower volatile content favours longer combustion duration since more fixed carbon is retained in
 303 the char for the torrefied biomass caused by the increase in C-C bonds during the decomposition of the
 304 lignocellulose component. Yet, the 45% reduction of VM for pinp does not lead to a significant difference
 305 with pine and pint as expected. This could be attributed to the higher interference between the two
 306 combustion phases and to the improved catalytic effect of ash in both torrefied fuels due to higher ash
 307 content. The role of volatile matter in accelerating the combustion is evident as the low volatile pinc takes
 308 up to three times more time to complete its oxidation. On top of rapid combustion of VM in the surrounding

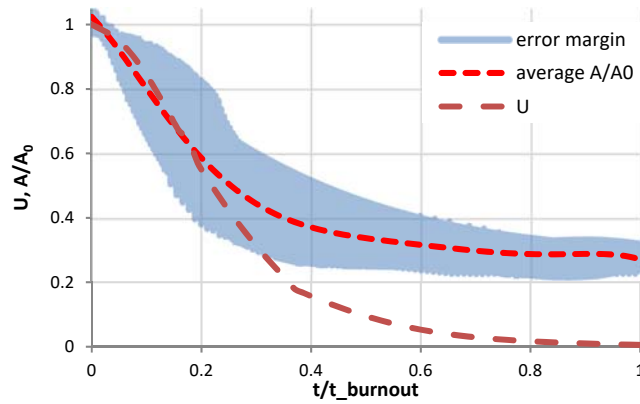
309 flame, volatile ejection deforms the particle and creates new pores in the char structure enhancing its
310 reactivity.

311 **4. Evolution of the projection area**

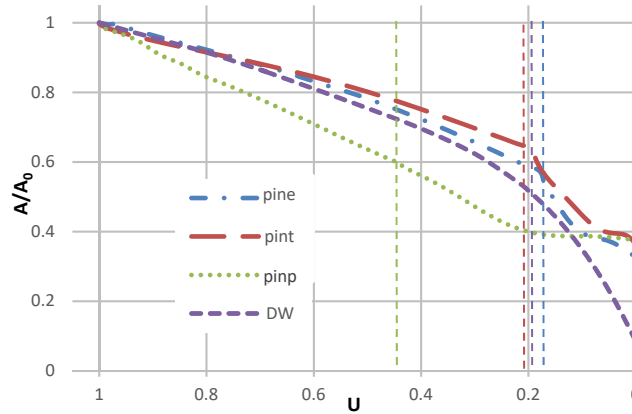
312 The evolution of the projection area gives an indication of the particle size evolution assuming
313 homogeneous and isotropic behaviour. In order to compare the area evolution of different particles, the
314 projection area is normalized by the initial projection area (at $t=0$) versus the normalized combustion time
315 t/t_{burnout} where t_{burnout} is the total combustion duration of each fuel type. On the other hand, the
316 unburnt fraction ($U = 1 - \text{consumed mass}/\text{initial mass}$) is also traced versus the normalized
317 combustion time. The unburnt fraction is obtained from combustion experiments of the samples performed
318 in a horizontal batch reactor at the same temperature (800°C), where similar combustion events and
319 durations are observed [24]. **Figure 9** shows the normalized area (A/A_0) of pine particles and their average
320 associated with the unburnt fraction (U) of pine vs the corresponding combustion time. The procedure is
321 repeated for every single particle and the result is the average of all curves. The coefficient of determination
322 (R^2) is higher than 0.9 for all fuel types. The variations between the particles are more pronounced during
323 the char combustion. Nevertheless, high similarity is found during the flame phase. The average curves of
324 each fuel are gathered in **Figure 10**. The rupture of each curve is the separation point of the flame and char
325 phase (represented as dashed lines in the graph). 44%, 37%, 40% and 46% of the initial projected area are
326 lost during the flame phase for pine, pint, pinp and DW respectively. The curves follow a power trend ($A =$
327 $A_0 U^\alpha$) for the flame part where α is the power coefficient listed in **Table 4** for each fuel. It is noticeable
328 that it gets higher with lower VM content except for torrefied pine Pint.

329 The table also includes the shrinking core model for char combustion that assumes a constant particle
330 density during char combustion. According to the model, char oxidation occurs in a diffusion controlled
331 process. The model depicts well the evolution of the reaction zone rather than the particle volume. DW char
332 is the closest to the model as it undergoes fragmentation during its oxidation and leaves little to no ash
333 matrix after the complete burnout. However, the other fuel chars follow the carbonized pine profile given
334 in **Figure 11**. The curve represents char oxidation in comparison with the shrinking particle model as a
335 function of the unburnt char fraction U_c , defined as the ratio of the remaining carbon to the fixed carbon
336 content. The model is fairly correct at the beginning of the char combustion but the data diverge later at the
337 point of separation of the two curves in **Figure 6** to an approximately constant volume as the combustion
338 progresses. Carbon is reacting with small variation of the external volume that ends with 33% to 39% of
339 the initial projection area after the complete burnout of all the fuel types except for DW with low ash
340 residue. Higher ash content accounted for larger ash matrix at the end. The char was sometimes swelling in
341 the course of its oxidation. This is obvious in the curve of carbonized pine that increases from $U_c \approx 0.3$ and
342 then shrinks again to reach 56% of its original shadow at the end. The swelling is probably caused by
343 trapped volatiles in the ash matrix (most likely lignin volatiles) that are liberated at the end because of the

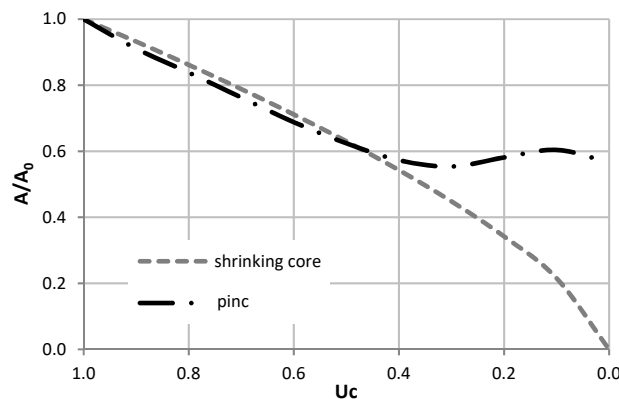
344 internal pressure increase. Ejections of particle fragments are also observed at the end when the particle
 345 swells. The phenomenon is notable for pint and it can be spotted by a slight increase in the slope of torrefied
 346 pine size as U approaches zero.



347
 348 **Figure 9:** Normalized area (A/A_0) and unburnt fraction (U) vs the normalized combustion time of pine



349
 350 **Figure 10:** Comparison of the projection area evolution as a function of the unburnt fraction of all fuels
 351 (U-axis in reverse order)



352
 353 **Figure 11:** Comparison between experimental char evolution and shrinking core model (U-axis in reverse
 354 order)

Fuel	Pine	Pint	Pinp	DW	Shrinking core
------	------	------	------	----	----------------

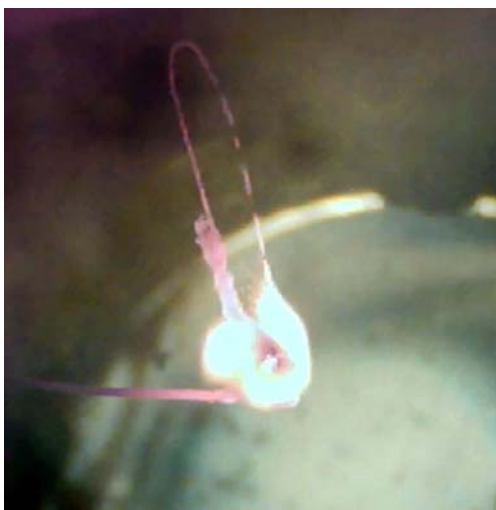
α	0.32	0.29	0.63	0.40	0.66
----------	------	------	------	------	------

355 **Table 4:** Exponent of power trend of area evolution
356 Assuming spherical particles and isotropic consumption, the particle volume can be directly evaluated from
357 its projection area. Even with initial irregular particle shape which rapidly tends to disappear and becomes
358 more rounded than the mother particle [22], [25].

359 **5. On the difference between biomass particle and coal particle combustion**

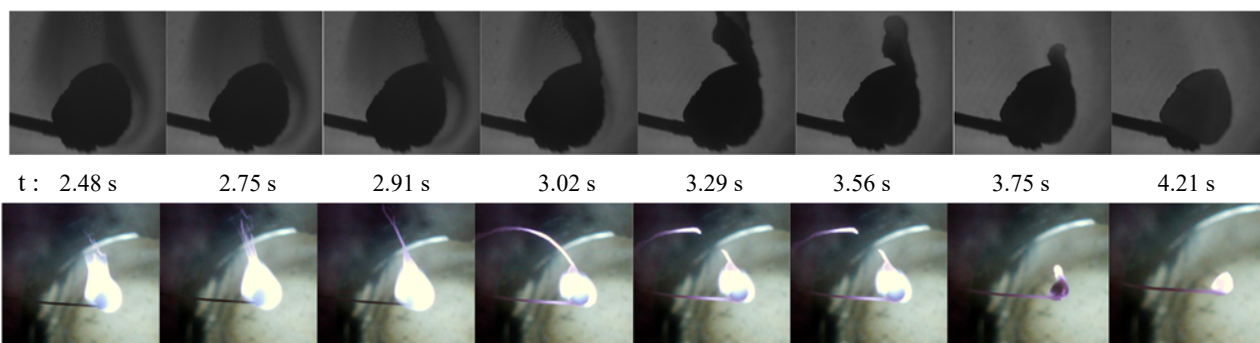
360 The difference between the combustion of coal and biomass is obviously demonstrated by the classical
361 characterization methods like TGA. These differences are the result of the physical and chemical variations
362 including density, composition (proximate and ultimate analysis), structure and porosity. The huge
363 difference in the volatile content is a prominent change that defines the flame characteristics and the char
364 properties. The chemical composition of the fuels is also different and the reaction is slower on coal due to
365 the difference of the intrinsic reactivity of the material as much as the surface area of the char [26]. Biomass
366 flames are transparent and possess uniform shape (near spherical) regardless of the particle irregular shape,
367 to the contrary of coal flames that are sooty and disturbed. The volatiles released from biomass consist
368 mostly of light hydrocarbons. Tars and heavy hydrocarbons crack expediently into light gases and pyrolytic
369 water before reacting with oxygen. Moreover, biomass volatiles have high oxygen proportion leading to
370 the formation of CO and CO₂. The latter inert gas dilutes the volatile cloud around the particle and reduces
371 the flame luminosity. In contrast, coal volatiles contain mostly heavy hydrocarbons and tars that appeared
372 to condense in a sooty contrail (**Figure 12**). Upon heating, the particle swells considerably indicating high
373 internal pressure due to lower porosity compared to biomass, which does not permit the volatiles to flow
374 out easily [27]. The pressure is relieved by brutal release of jets containing dense species that cast a shadow
375 in the monochrome video. The dense trails are precursors of soot formation so they condense and
376 agglomerate to develop a contrail of intense luminosity inside the flame. It can be distinguished from the
377 flame by its high luminosity while entraining the flame in a large fluctuation. The condensed material
378 extends outwards to a long distance forming a bright tail. The contrail sometimes bends back to the particle
379 forming a closed loop (**Figure 12**) or extends long to the point that it cannot be held by the particle causing
380 its far end to bend and break (**Figure 13**). Since more time is needed to oxidize tars especially in low oxygen
381 environment like the flame, the attached condensed structure persists after the flame extinction and
382 undergoes oxidation to disappear gradually in less than a second. The same phenomenon is reported for
383 bituminous coal in [28][29][2][30]. The flame is followed by a bright particle that burns gradually.

384 The high magnification of the shadowgraph videos allows observing in details the combustion taking place
385 on the surface of the particle. Note that the heterogeneous combustion of coal is maintained mostly at
386 constant temperature. At the beginning of the char combustion, the particle appears barely compared to the
387 soot contrail. As the burning time goes by, the oxidation reaction intensifies and the char glowing as well.



388
389

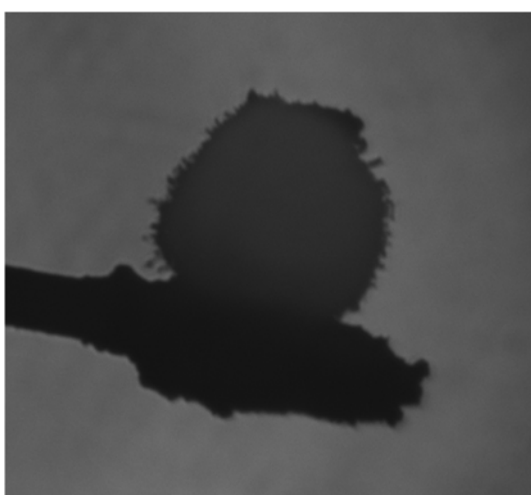
Figure 12: Soot contrail forming closed loop during coal particle combustion



390

391

Figure 13: Selected images from the high magnification monochrome camera and the corresponding direct emission camera showing the formation and disappearance of the condensed material (insertion at $t=0$ sec) during combustion of a single Venezuelan coal particle (1.6 mg)



395

Figure 14: Heterogeneous combustion of a coal particle with some filaments appearing on the surface

397 Some chars burn with constant volume where oxygen penetrates the cenosphere interior through the pores
398 and the combustion continues internally similar to the biomass char combustion. In this case, the particle
399 glow fades slowly as the combustion proceeds internally. However, the particle volume shrinks most of the
400 time, with small filaments appearing on the displaced surface (**Figure 14**). The formation of filaments has
401 been also detected by Olsbye et al. on coke formed during methane-to-synthesis gas reactions [31]. These
402 filaments are distributed radially at the surface, and thereafter, separate from the char as fly ash. Due to
403 lower reactivity and higher fixed carbon in coal, the biomass char burns up to five times faster than coal.
404 This also applies for biomass with comparable volatile matter and fixed carbon content as coal. For
405 example, pinp with about 52% FC burns four times faster than the 61% FC coal. This is addressed by the
406 faster char gasification reactions induced by the higher oxygen to carbon ratio in biomass char [32]. It is
407 also attributed to enhanced catalytic role of alkali metals in biomass chars due to higher concentration [33].

408 **Conclusion**

409 The combustion of single particles of raw and torrefied pine, demolition wood and coal is studied using
410 simultaneous shadowgraphy and direct emission imaging techniques, allowing detailed investigation of the
411 combustion events at the particle level. It gives insight to the phenomena occurring at the particle surface
412 and around it during the whole process, including the onset of heterogeneous ignition and the volume and
413 shape evolution. The results verify the important role of the VM content and particle size in determining
414 the combustion intensity and durations. Higher VM particles undergo intense devolatilisation for
415 comparable durations as less volatile containing fuel. The flame duration appears to be more influenced by
416 the particle size than the particle volatile content. This leads to more intense combustion for higher VM
417 particles that obstructs the oxygen diffusion to the particle and delays the heterogeneous ignition. On the
418 other hand, the char left is more reactive and burn faster than the char resulting from particles with lower
419 VM content. A char resulting from a particle with no initial VM burns three times slower than its raw
420 counterpart. On the other hand, larger particles mean slower temperature rise before and after ignition and
421 lower devolatilisation intensity. This, beside the larger surface area, increases the probability of earlier
422 heterogeneous ignition and longer overlap.

423 The projection area evolution is traced versus the burnout using gas emission results. VM occupy around
424 40% of the initial particle shadow which decreases with devolatilisation progress following a power trend.
425 The power coefficient doubles with intense pre-treatment of the fuel. The latter leads to increase the char
426 volume, which shrinks after the flame end following the shrinking core model. But it diverges later to a
427 constant residual ash volume, which increases with more intense pre-treatment. An empirical model can be
428 extracted from the curves assuming spherical particles. The volume evolution obtained by shadowgraphy
429 will be integrated in a 1-D solid combustion model developed and validated for different compositions and
430 preparations of biomass. A comparison between biomass and coal shows the visual differences of the gas
431 phase composition and the char structure giving rise to differences in the flame and char combustion of
432 both fuels.

- 433
434 **Acknowledgments**
435 The financial support of ANRT for H. Mohanna's PhD scholarship is acknowledged (Convention CIFRE - N°
436 2016/0523).
- 437 **References**
- 438 [1] J. Riaza, J. Gibbins, and H. Chalmers, "Ignition and combustion of single particles of coal and biomass," *Fuel*, vol. 202,
439 pp. 650–655, Aug. 2017.
- 440 [2] J. Riaza *et al.*, "Single particle ignition and combustion of anthracite, semi-anthracite and bituminous coals in air and
441 simulated oxy-fuel conditions," *Combust. Flame*, vol. 161, no. 4, pp. 1096–1108, Apr. 2014.
- 442 [3] J. Riaza *et al.*, "Combustion of single biomass particles in air and in oxy-fuel conditions," *Biomass and Bioenergy*, vol.
443 64, pp. 162–174, May 2014.
- 444 [4] E. Marek and K. Stańczyk, "Case Studies Investigating Single Coal Particle Ignition and Combustion," *J. Sustain. Min.*,
445 vol. 12, no. 3, pp. 17–31, 2013.
- 446 [5] N. Vorobiev and M. Schiemann, "Determination of Char Combustion Kinetics of Torrefied Biomass by Use of
447 Stereoscopic Pyrometry," in *40th International Technical Conference Clean Coal Fuel System*, 2015.
- 448 [6] Maryam Momeni, "Fundamental Study of Single Biomass Particle Combustion," Aalborg University, 2012.
- 449 [7] Z. Lu, J. Jian, P. A. Jensen, H. Wu, and P. Glarborg, "Influence of Torrefaction on Single Particle Combustion of
450 Wood," *Energy & Fuels*, vol. 30, no. 7, pp. 5772–5778, Jul. 2016.
- 451 [8] H. Lu, E. Ip, J. Scott, P. Foster, M. Vickers, and L. L. Baxter, "Effects of particle shape and size on devolatilization of
452 biomass particle," *Fuel*, vol. 89, no. 5, pp. 1156–1168, May 2010.
- 453 [9] E. Houshfar, L. Wang, N. Vähä-Savo, A. Brink, and T. Lövås, "Experimental Study of a Single Particle Reactor at
454 Combustion and Pyrolysis Conditions," *CHEMICAL ENGINEERING Trans.*, vol. 35, pp. 613–618, 2013.
- 455 [10] M. Schiemann, S. Haarmann, and N. Vorobiev, "Char burning kinetics from imaging pyrometry: Particle shape effects,"
456 *Fuel*, vol. 134, pp. 53–62, Oct. 2014.
- 457 [11] P. E. Mason, L. I. Darvell, J. M. Jones, M. Pourkashanian, and A. Williams, "Single particle flame-combustion studies
458 on solid biomass fuels," *Fuel*, vol. 151, pp. 21–30, Jul. 2015.
- 459 [12] J. Brix, P. A. Jensen, and A. D. Jensen, "Modeling char conversion under suspension fired conditions in O₂/N₂ and
460 O₂/CO₂ atmospheres," *Fuel*, vol. 90, no. 6, pp. 2224–2239, Jun. 2011.
- 461 [13] J. Andrzejewski, A. Charlet, P. Higelin, A. Sapinski, and G. Vaitilingom, "Procédé et dispositif de mesure de la vitesse
462 d'évaporation et du délai d'inflammation d'un carburant liquide .," FR2694092 A1.
- 463 [14] Sternberg, "Biomedical Image Processing," *Computer (Long. Beach. Calif.)*, vol. 16, no. 1, pp. 22–34, Jan. 1983.
- 464 [15] "https://imagej.net/Auto_Threshold#Try_all."
- 465 [16] T. Daho *et al.*, "Study of droplet vaporization of various vegetable oils and blends of domestic fuel oilcottonseed oil
466 under different ambient temperature conditions," *Biomass and Bioenergy*, vol. 46, pp. 653–663, 2012.
- 467 [17] J. F. Saldarriaga, R. Aguado, A. Pablos, M. Amutio, M. Olazar, and J. Bilbao, "Fast characterization of biomass fuels by
468 thermogravimetric analysis (TGA)," *Fuel*, vol. 140, pp. 744–751, Jan. 2015.
- 469 [18] J. Li, M. C. Paul, and K. M. Czajka, "Studies of Ignition Behavior of Biomass Particles in a Down-Fire Reactor for
470 Improving Co-firing Performance," *Energy & Fuels*, vol. 30, no. 7, pp. 5870–5877, Jul. 2016.
- 471 [19] E. Gucho, K. Shahzad, E. Bramer, N. Akhtar, and G. Brem, "Experimental Study on Dry Torrefaction of Beech Wood
472 and Miscanthus," *Energies*, vol. 8, no. 5, pp. 3903–3923, May 2015.
- 473 [20] F. S. Akinrinola, "Torrefaction and Combustion Properties of some Nigerian Biomass," The University of Leeds, 2014.
- 474 [21] T. G. Bridgeman, J. M. Jones, I. Shield, and P. T. Williams, "Torrefaction of reed canary grass, wheat straw and willow
475 to enhance solid fuel qualities and combustion properties," *Fuel*, vol. 87, no. 6, pp. 844–856, May 2008.
- 476 [22] A. Panahi, Y. A. Levendis, N. Vorobiev, and M. Schiemann, "Direct observations on the combustion characteristics of
477 Miscanthus and Beechwood biomass including fusion and spherodization," *Fuel Process. Technol.*, vol. 166, pp. 41–49,
478 Nov. 2017.
- 479 [23] C. Mock, H. Lee, S. Choi, and V. Manovic, "Combustion Behavior of Relatively Large Pulverized Biomass Particles at
480 Rapid Heating Rates," *Energy & Fuels*, vol. 30, no. 12, pp. 10809–10822, Dec. 2016.
- 481 [24] Brice Piednoir, "Comportement en combustion de résidus de biomasse : mise en évidence de synergies par mélange sous
482 forme de granulés," Thèse Université de Perpignan Via Domitia, 2017.
- 483 [25] C. Meesri and B. Moghtaderi, "Experimental and numerical analysis of sawdust-char combustion reactivity in a drop
484 tube reactor," *Combust. Sci. Technol.*, vol. 175, no. 4, pp. 793–823, Apr. 2003.
- 485 [26] M. V. Gil, J. Riaza, L. Álvarez, C. Pevida, J. J. Pis, and F. Rubiera, "Kinetic models for the oxy-fuel combustion of coal
486 and coal/biomass blend chars obtained in N₂ and CO₂ atmospheres," *Energy*, vol. 48, no. 1, pp. 510–518, 2012.
- 487 [27] M. V. Gil, J. Riaza, L. Álvarez, C. Pevida, J. J. Pis, and F. Rubiera, "Oxy-fuel combustion kinetics and morphology of
488 coal chars obtained in N₂ and CO₂ atmospheres in an entrained flow reactor," *Appl. Energy*, vol. 91, no. 1, pp. 67–74,
489 Mar. 2012.
- 490 [28] W. J. McLean, D. R. Hardesty, and J. H. Pohl, "Direct observations of devolatilizing pulverized coal particles in a
491 combustion environment," *Symp. Combust.*, vol. 18, no. 1, pp. 1239–1248, 1981.
- 492 [29] R. Khatami, C. Stivers, and Y. A. Levendis, "Ignition characteristics of single coal particles from three different ranks in
493 O₂/N₂ and O₂/CO₂ atmospheres," *Combust. Flame*, vol. 159, no. 12, pp. 3554–3568, Dec. 2012.
- 494 [30] E. Marek and B. Świątkowski, "Experimental studies of single particle combustion in air and different oxy-fuel
495 atmospheres," *Appl. Therm. Eng.*, vol. 66, no. 1–2, pp. 35–42, May 2014.
- 496 [31] U. Olsbye, O. Moen, Å. Slagtern, and I. M. Dahl, "An investigation of the coking properties of fixed and fluid bed
497 reactors during methane-to-synthesis gas reactions," *Appl. Catal. A Gen.*, vol. 228, no. 1–2, pp. 289–303, Mar. 2002.

- 498 [32] K. Matsumoto, K. Takeno, T. Ichinose, T. Ogi, and M. Nakanishi, "Gasification reaction kinetics on biomass char
499 obtained as a by-product of gasification in an entrained-flow gasifier with steam and oxygen at 900–1000°C," *Fuel*, vol.
500 88, no. 3, pp. 519–527, Mar. 2009.
- 501 [33] P. Ollero, A. Serrera, R. Arjona, and S. Alcantarilla, "The CO₂ gasification kinetics of olive residue," *Biomass and*
502 *Bioenergy*, vol. 24, no. 2, pp. 151–161, Feb. 2003.